

# Dynamics of stream-subhalo interactions

Jason L. Sanders<sup>1\*</sup>, Jo Bovy<sup>2</sup> and Denis Erkal<sup>1</sup>

<sup>1</sup>Institute of Astronomy, Madingley Road, Cambridge, CB3 0HA

<sup>2</sup>Department of Astronomy and Astrophysics, University of Toronto, 50 St. George Street, Toronto, ON M5S 3H4

23 September 2015

## ABSTRACT

We develop a formalism for modelling the impact of dark matter subhaloes on cold thin streams. Our formalism models the formation of a gap in the stream in angle-frequency space and is able to handle general stream and impact geometry. We analyse a single simulation in angle-frequency space and demonstrate that our formalism is able to predict the gap properties at a range of times. We show how the results in angle-frequency space can be related to physical properties of the gaps and that previous results for more constrained simulations are recovered.

We demonstrate how our results are dependent upon the mass of the subhalo and the location of the impact along the stream. We find that gaps formed far downstream grow more rapidly than those closer to the progenitor due to the ordered nature of the stream. Additionally, we find that the minimum gap density plateaus in time at a value that decreases with increasing subhalo mass.

We provide general expressions for the velocity perturbations due to the fly-by of a Plummer and a Hernquist sphere.

## Key words:

## 1 INTRODUCTION

One of the key predictions of the currently favoured  $\Lambda$ CDM cosmology is hierarchical structure formation. Early in the Universe dark matter overdensities formed, began accumulating baryons and conglomerating into ever larger dark matter haloes. The result of this process is that at the current time within a large dark matter halo such as that of the Milky Way there are many smaller dark matter haloes. Current simulations (Diemand et al. 2008; Springel et al. 2008) predict there are a spectrum of these subhaloes.

From an observational point-of-view the nature of dark matter has remained aloof as direct detection has proved fruitless. The other crucial line of attack is probing the gravitational effects of dark matter on both visible matter and photons on astrophysical scales. The large-scale smooth dark matter halo is being mapped out with dynamical models of both the assumed phase-mixed components of the Galaxy (e.g. the disc REF and the stellar halo REF) and those components of the Galaxy that are yet to fully phase mix (e.g. tidal streams REF). Tidal streams are filaments of material stripped from satellites of a host Galaxy and are naturally a result of the hierarchical structure formation picture. Some streams (e.g. GD-1, Palomar 5) are observed to be very kinematically cold such that, in addition to being probes of the large-scale dark matter structure, they are very sensitive probes of interactions with the dark matter subhaloes. Interactions between streams and dark matter haloes produce gaps in the streams that grow over time. A con-

clusive detection of one such a gap would be very powerful evidence for  $\Lambda$ CDM cosmology, whilst the ultimate goal might be to measure the dark-matter halo mass spectrum from a whole series of observed gaps.

To achieve this ambitious goal we need a concerted modelling effort to understand the structure of a gap in a stream. The goal is doubly ambitious due to the difficulties that modelling unperturbed streams has presented. The modelling of streams has received considerable attention in the literature and there have been many proposed methodologies for measuring the Galactic potential using streams. However, there have been relatively few successful applications to the data (Koposov et al. 2010; Law & Majewski 2010; Gibbons et al. 2014; Küpper et al. 2015; Bowden et al. 2015) and we have not yet reached a point where modelling a stream is simple. One very powerful method is to construct models of streams in angle-frequency space as proposed by Bovy (2014) and Sanders (2014). This space simplifies the stream dynamics (Helmi & White 1999; Tremaine 1999) and allows rapid generation of general stream models.

In recent years there has been much progress made in understanding the structure of stream gaps through the analysis of numerical simulations (Siegal-Gaskins & Valluri 2008; Carlberg 2009; Yoon et al. 2011; Carlberg 2012) as well as through analytic approaches (Carlberg & Grillmair 2013; Erkal & Belokurov 2015a,b). The analytic approaches have relied heavily on the simplicity with which circular orbits can be handled. Unfortunately, by their nature tidal streams are on more eccentric orbits such that these approaches, whilst providing useful insight, seem too simplistic to

\* E-mail: jls@ast.cam.ac.uk

tackle any data. In this paper we will build on the angle-frequency stream formalism and argue that it provides a clear basis on which to incorporate perturbations due to subhalo fly-bys. We show that many of the insights from circular orbits can be extended to general, eccentric orbits. We work from the point-of-view that we know the underlying unperturbed stream model well and we are trying to characterise substructure in the stream.

We will show how one can compute the kicks in velocity, angles and frequencies for general subhaloes and general impact geometries. We provide analytic forms for the computation of the kicks in velocity for both Plummer and Hernquist subhaloes. With the aid of a simulation of a cold stream on an eccentric orbit in a flattened axisymmetric logarithmic potential we demonstrate how a perturbed stream model can be generated and we inspect the resultant distributions in action, angle and frequency space. We show that a gap forms in angle, frequency and action space and that the gap size in the parallel angle space (the angle along the stream) grows like the spatial gap size. We simulate a series of halo fly-bys of differing masses and geometry. We find in all cases the minimum density in the gap plateaus in time and that the gap size grows fastest for fly-bys far from the stream progenitor where the particles are well ordered by energy.

The paper is arranged as followed. We begin in Section 2 with the framework for computing the perturbation of a stream due to a general subhalo fly-by. In Section 3 we detail a simulation of a  $10^8 M_\odot$  dark matter impact on a cold stream formed from a progenitor on an eccentric orbit. We apply the framework of Section 2 to understand the structure of the simulation and show we are able to reliably simulate the fly-by. In Section 4 we simulate fly-bys of varying subhalo masses and varying impact geometry. We discuss the applicability of our formalism in Section ?? before closing with our conclusions in Section 6.

## 2 FORMALISM

### 2.1 Velocity kicks

In this section we give expressions for the velocity changes of stream particles under the influence of a subhalo fly-by. Following Yoon et al. (2011), Carlberg & Grillmair (2013) and Erkal & Belokurov (2015a) we work under the impulse approximation i.e. the integrated acceleration is assumed to act instantaneously at some impact time such that the velocity of the stream particles changes instantly. The change in velocity is given by

$$\delta\mathbf{v} = \int_{-\infty}^{\infty} dt \mathbf{a}(\mathbf{x}(t)), \quad (1)$$

where  $\mathbf{a}$  is the acceleration resulting from the force exerted by the subhalo which depends on the location  $\mathbf{x}$  of the particle at time  $t^1$ . The fly-by is described by the impact parameter  $b$ , the velocity of the subhalo  $\mathbf{w}$  and the time of the impact  $t = -t_g$ . To simplify the following expressions we set  $t_g = 0$ . Erkal & Belokurov (2015a) gave expressions for the velocity kicks due to a Plummer subhalo on a straight stream segment moving at a fixed relative velocity to the subhalo. If we consider the example of GD-1 and take the model of Koposov et al. (2010) we find that the observed segment of the stream has a radius of curvature of  $\sim 24$  kpc. We will see that for

<sup>1</sup> Throughout this paper we use  $\delta$  to denote changes in quantities for individual particles in time e.g. from the subhalo fly-bys, and  $\Delta$  for differences between particles.

a  $10^8 M_\odot$  Plummer subhalo with scale radius  $r_s = 0.625$  kpc the kicks are important on scales of  $\sim 10r_s \approx 6$  kpc such that the radius of curvature is comparable to the region over which the kick is important. Similarly, the typical distance a stream particle moves during the interaction is  $\sim 10|\mathbf{v}|r_s/|\mathbf{w} - \mathbf{v}| \approx 10r_s/\sqrt{2} \approx 4$  kpc (where  $\mathbf{w}$  is the velocity of the subhalo) such that the curvature of the motion of an individual particle is also important over the interaction. Here we will give more general formulae for the velocity kicks that account for the curved extent of the stream.

We expand on the formalism of Erkal & Belokurov (2015a) by explicitly considering the spatial distribution of the stream. We retain the simplification that each particle moves at a fixed relative velocity to the subhalo during the fly-by. We define the phase-space coordinates of the stream particles as  $(\mathbf{x}_i, \mathbf{v}_i)$  and the stream point of closest approach as  $(\mathbf{x}_0, \mathbf{v}_0)$ . The vector of closest approach is given by

$$\mathbf{b}_0 = b \frac{\mathbf{w} \times \mathbf{v}_0}{|\mathbf{w} \times \mathbf{v}_0|}. \quad (2)$$

Note the sign of  $b$  is important in defining the curvature of the stream relative to the subhalo. We define

$$\mathbf{b}_i = \mathbf{b}_0 + \mathbf{x}_i - \mathbf{x}_0 \quad (3)$$

as the displacement vector between stream particle  $i$  and the subhalo at the impact time, and

$$\mathbf{w}_i = \mathbf{w} - \mathbf{v}_i \quad (4)$$

as the corresponding relative velocity. The expression for the velocity kicks for the  $i$ th stream particle is given by

$$\delta\mathbf{v}_i^g = \int_{-\infty}^{\infty} dt \mathbf{a}(\mathbf{x}(t)), \quad (5)$$

$$\mathbf{x}(t) = \mathbf{b}_i + \mathbf{w}_i t.$$

For general subhalo acceleration fields this integral must be calculated numerically via a coordinate transformation to make the limits finite. However, for both a Plummer subhalo and a Hernquist subhalo the velocity kicks may be computed analytically. The potential of a Plummer sphere is given by

$$\Phi_P(r) = -\frac{GM}{\sqrt{r^2 + r_s^2}}, \quad (6)$$

where  $M$  is the mass and  $r_s$  the scale radius. The velocity kicks are given by

$$\delta\mathbf{v}_{i,P}^g = -\frac{2GM}{|\mathbf{w}_i|} \frac{\mathbf{b}_i - \hat{\mathbf{w}}_i (\mathbf{b}_i \cdot \hat{\mathbf{w}}_i)}{(B^2 + r_s^2)}, \quad (7)$$

where

$$B^2 = |\mathbf{b}_i|^2 - |\mathbf{b}_i \cdot \hat{\mathbf{w}}_i|^2. \quad (8)$$

In Fig. 1 we show a comparison between the kicks calculated using approaches of increasing complexity. We compute the kicks calculated assuming the stream is a straight-line segment as in Erkal & Belokurov (2015a), the kicks calculated using the curvature of the stream track as in equation (7), the kicks calculated using the full orbital path of each stream particle but assuming the subhalo moves in a straight line, and finally the kicks calculated using the full orbit of the stream particles *and* the subhalo. The last of these is computed by first integrating each particle and the subhalo backwards in time for some time  $T$  in the galactic potential, integrating the particles forward in the combined galactic and subhalo potentials for a time  $2T$  and finally integrating the particles backwards for a time  $T$  and computing the difference between the initial and final velocities.

The particles are evolved in a flattened logarithmic potential of the form

$$\Phi_L(R, z) = \frac{V_c^2}{2} \log \left( R^2 + \frac{z^2}{q^2} \right), \quad (9)$$

with  $V_c = 220 \text{ km s}^{-1}$  and  $q = 0.9$ , and the stream here is modelled simply as a circular orbit at 10 kpc with a circular velocity of  $220 \text{ km s}^{-1}$  impacted by a Plummer sphere of velocity  $\mathbf{w} = (0, 132, 176) \text{ km s}^{-1}$  and impact parameter  $b = 625 \text{ pc}$ . We show two kicks: one due to a subhalo of mass  $10^8 M_\odot$  and scale radius  $r_s = 625 \text{ pc}$  and one due to a subhalo of mass  $10^7 M_\odot$  and scale radius  $r_s = 250 \text{ pc}$ . The distance along the stream in the straight-line approximation is calculated as  $\Delta\phi \times 10 \text{ kpc}$ . The differences are small. One very noticeable difference is the  $\delta v_x^g$  kicks computed using the orbital path of the stream particles, but with the sub-halo moving in a straight line, is significantly larger than for the other three cases. This is because the stream particles curve towards the sub-halo track and so experience an increase perturbation. This picture is confirmed by moving the sub-halo fly-by to outside the stream track which produces an under-estimate for  $|\delta v_x^g|$ . Additionally the  $\delta v_z^g$  kicks for the full stream and subhalo integration are smaller at large distances from the closest approach. We also show  $\mathbf{v} \cdot \delta \mathbf{v}^g$  which is very similar for the four cases. As we will see later it is this quantity which has the largest effect on the future structure of the stream. For our calculations in Section ?? we will use equation (7) to calculate all kicks.

We also consider kicks due to Hernquist profiles (as with the Plummer profile the kicks can be computed analytically as shown in Appendix A) and truncated Navarro-Frenk-White (NFW) profiles. The density profile for the truncated NFW halo is given by

$$\rho_{\text{NFW}}(r) = \frac{M}{4\pi r_s^3} \left( \frac{r}{r_s} \right)^{-1} \left( 1 + \frac{r}{r_s} \right)^{-2} \operatorname{sech} \left( \frac{r}{r_t} \right). \quad (10)$$

$r_t$  is the truncation radius. For non-zero  $r_t$  the forces and potential must be computed numerically and clearly for  $r_t \rightarrow \infty$  the form reduces to the well-known NFW profile.

In Fig. 2 we show the kicks computed for a Plummer subhalo, a Hernquist subhalo, a NFW subhalo and truncated NFW subhalo. We also show  $\mathbf{v} \cdot \delta \mathbf{v}^g$  which is the quantity that controls the future structure of the stream. We have assumed the stream is a straight-line segment moving along the  $y$  axis at velocity  $v_y$ . The Plummer subhalo has a scale-radius  $r_s$  and satisfies  $4GM = r_s v_y^2$ . The other two finite-mass haloes have the same total mass as the Plummer sphere, with the NFW halo mass parameter chosen to be equal to the total mass of the Plummer sphere. All haloes have scale radii chosen such that the mass contained within  $r_s$  is identical to the enclosed mass for the Plummer sub-halo. This results in scale radii given by  $r_{s,\text{Hernquist}} = 1.36r_s$ ,  $r_{s,\text{NFW}} = 1.21r_s$ ,  $r_{s,\text{NFWtrunc}} = 1.76r_s$ . The truncated NFW profile has a truncation radius of  $r_t = 2r_{s,\text{NFWtrunc}}$ . We also show, for reference, the kicks from a point-mass, or Kepler potential, with mass equal to the mass enclosed by the Plummer sphere at  $r_s$ . The subhaloes have velocity  $\mathbf{w} = (0.3, 0.6, 0)v_y$  and impact parameter  $b = \sqrt{3}/2r_s$ .

The Plummer sphere produces the smallest kicks as it has the least mass at small radii, whilst the Kepler potential is the most concentrated and produces the largest kicks. The Hernquist sphere produces the second smallest kicks as the mass enclosed for  $r_s < r < 10r_s$  is smallest for the Hernquist sphere. As expected the NFW and truncated NFW profiles produce similar amplitude kicks at small distances but the truncated NFW kicks fall off faster at larger distances. The NFW profile is most spatially extended so it produces the largest kicks at large distances. However, such a

dark matter subhalo is unphysical so we only include it here for completeness. The four finite mass subhaloes produce kicks that tend towards each other at large distances.

## 2.2 Angle-frequency kicks

Erkal & Belokurov (2015a) gave analytic results for the structure of a gap as a function of time for streams on circular orbits. Such an approach is fruitful for developing an understanding of the gap formation but when modelling realistic streams we require a formalism that is appropriate for eccentric orbits. Dynamical systems are often simplified through the use of angle-actions coordinates ( $\mathbf{J}, \boldsymbol{\theta}$ ). These canonical coordinates possess the properties that the actions are integrals of motion whilst the angles increase linearly with time at a constant rate  $\boldsymbol{\Omega}$ , which are the frequencies. The equations of motion for the angle-action coordinates are

$$\begin{aligned} \mathbf{J} &= \text{const.}, \\ \boldsymbol{\theta} &= \frac{\partial H}{\partial \mathbf{J}} t + \boldsymbol{\theta}(0) = \boldsymbol{\Omega} t + \boldsymbol{\theta}(0), \end{aligned} \quad (11)$$

where  $t$  is the time and  $\boldsymbol{\theta}(0)$  is the angle at  $t = 0$ . In axisymmetric potentials<sup>2</sup> the three actions are given by  $\mathbf{J} = (J_R, L_z, J_z)$ .  $J_R$  is the radial action describing the extent of the radial oscillations,  $J_z$  is the vertical action describing the extent of the vertical oscillations and  $L_z$  is the  $z$ -component of the angular momentum. To compute the actions, angles and frequencies in this paper we use the method detailed by both Sanders & Binney (2014) and Bovy (2014). This method uses a generating function to transform from a set of toy angle-action variables (computed in an isochrone potential) to the target set. The coefficients of the generating function (Fourier components  $S_n$  and their derivatives) are found from a least-squares fit to a series of phase-space samples from an orbit integration.

The angle-action coordinates simplify the description of the evolution of a tidal stream, as once stripped the stream members move essentially as free particles in the galactic potential. Helmi & White (1999) and Tremaine (1999) both discussed the evolution of a stream as a small action clump in angle-actions, which was further built on by the work of Eyre & Binney (2011). Sanders & Binney (2013b) presented the idea that the angle-frequency distribution could be used as a probe of the galactic potential. These ideas were extended by both Bovy (2014) and Sanders (2014) who developed generative models for streams in angle-frequency space. This framework is ideal for the introduction of velocity perturbations due to a subhalo.

Each particle in a stream obeys the equation

$$\Delta \boldsymbol{\theta} = \boldsymbol{\theta} - \boldsymbol{\theta}_0 = (\boldsymbol{\Omega} - \boldsymbol{\Omega}_0)t_s + \Delta \boldsymbol{\theta}_{\text{init}} = \Delta \boldsymbol{\Omega}_{\text{init}} t_s + \Delta \boldsymbol{\theta}_{\text{init}}, \quad (12)$$

where the subscript 0 denotes the coordinates of the progenitor,  $\Delta$  denotes separation between the progenitor and a stream particle and the subscript ‘init’ denotes the separation between progenitor and particle at release and  $t_s$  is the time since the particle was stripped. This means  $\Delta \boldsymbol{\Omega}$  is the separation in frequencies between a stream particle and the progenitor, which is constant after the particle has been stripped, and  $\Delta \boldsymbol{\theta}$  is the separation in angles between a stream particle and the progenitor which grows linearly in time at a rate  $\Delta \boldsymbol{\Omega}$ .

A long thin stream is characterised by a vector  $\mathbf{n}$  along which

<sup>2</sup> In this paper we will only work with axisymmetric potentials but the formalism is simply extended to more general potentials.

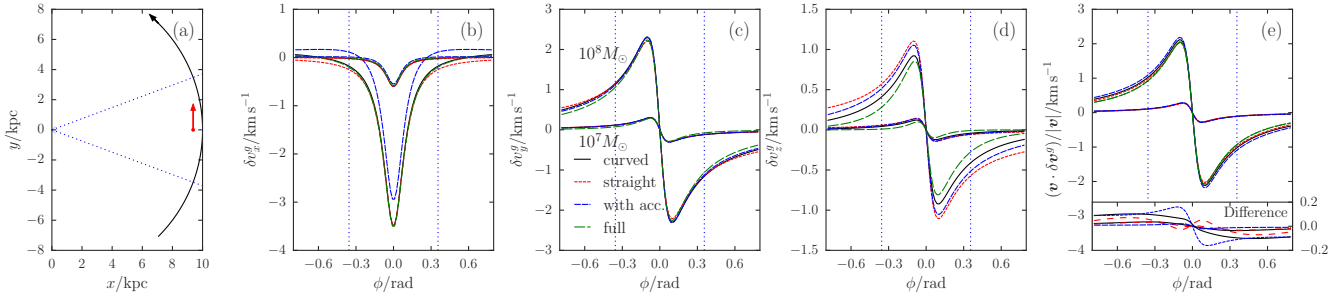


**Figure 1.** A comparison of the velocity kicks calculated with varying levels of complexity. **Panel (a):** The stream track is a circular orbit of radius 10 kpc and circular velocity  $220 \text{ km s}^{-1}$  and is shown in black in the left panel. Two lines are shown in the second through to fifth panel corresponding to two subhaloes, which are each a Plummer sphere moving at  $\mathbf{w} = (0, 132, 176) \text{ km s}^{-1}$  with an impact parameter  $b = 625 \text{ pc}$ . The red arrow in the left panel shows the projection of the velocity vector into the plane. The higher amplitude kicks correspond to the sphere of mass  $10^8 M_\odot$  and scale radius  $r_s = 625 \text{ pc}$  and the lower amplitude kicks correspond to the sphere of mass  $10^7 M_\odot$  and scale radius  $r_s = 250 \text{ pc}$ . **Panels (b), (c) & (d):** The second, third and fourth plots show the velocity kicks as a function of the azimuthal angle from the centre of the galaxy. The black lines show the kicks calculated using equation (7) (i.e. fixed relative velocity during fly-by), whilst the red short-dashed lines show the kicks computed assuming the stream is a straight line segment along the  $y$ -axis, the blue medium-dashed line shows the kicks computed using the full path of each particle during the fly-by and the green long-dashed lines show the kicks computed by integrating each particle in the combined galactic and orbiting Plummer potential. **Panel (e):** The rightmost panel shows  $\mathbf{v} \cdot \delta\mathbf{v}^g$  with the small inset showing the difference between the lines. The black line shows the difference between the full computation and the kicks computed with equation (7), the red short-dashed line shows the difference between the full computation and the kicks computed assuming the stream is a straight line, and the blue long-dashed shows the difference between the full computation and that including the acceleration of each particle during the fly-by. The dotted blue lines show the angles at which the projection of the velocity vector of the subhalo intersects the stream.

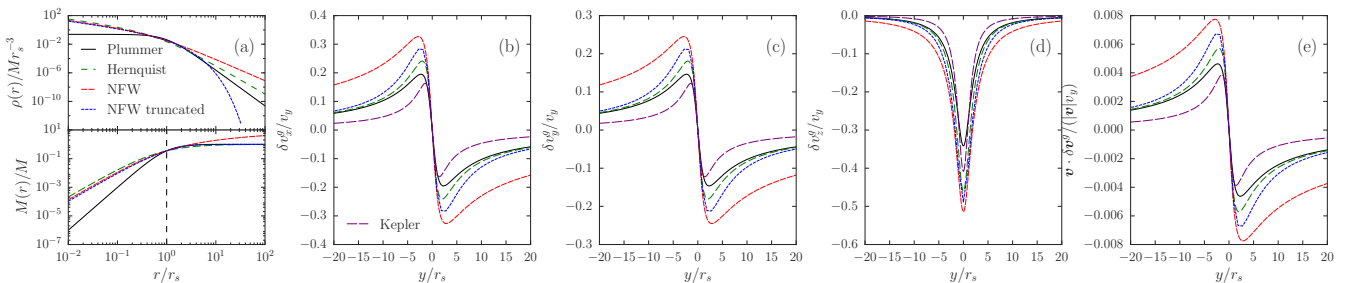


**Figure 2.** A comparison of the velocity kicks from a Plummer (black solid), a Hernquist (green long-dashed), a NFW (red medium-dashed) and a truncated NFW subhalo (blue short-dashed). **Panel (a):** The left panel shows the density (top) and mass (bottom) profiles of the four haloes. The three finite mass haloes have the same total mass and the NFW profile has the same mass parameter. The Hernquist, NFW and truncated NFW scale radii are chosen such that at the Plummer scale radius ( $r_s$ ) the same mass is enclosed by the profiles. The truncated NFW halo has a truncation radius equal to twice its scale radius. **Panels (b), (c) & (d):** The second, third and fourth panels show the velocity kicks as a function of the distance along the stream. **Panel (e):** The rightmost panel shows  $\mathbf{v} \cdot \delta\mathbf{v}^g$ . The stream is a particle train along the  $y$ -axis with velocity  $v_y$ . The subhaloes have  $4GM = r_s v_y^2$ ,  $r_{s,\text{Hernquist}} = 1.36r_s$ ,  $r_{s,\text{NFW}} = 1.21r_s$ ,  $r_{s,\text{NFWtrunc}} = 1.76r_s$ , impact parameter  $b = \sqrt{3}/2r_s$  and velocity  $\mathbf{w} = (0.3, 0.6, 0)v_y$ . In the second through fifth panel we show in long-dashed purple the kicks from a point-mass (or Kepler potential) with mass equal to the enclosed mass of the Plummer halo at the scale radius.

the particles lie in both angle and frequency space. Under the assumption of an isotropic action distribution this vector is the principal eigenvector of the Hessian matrix  $D_{ij} = \partial^2 H / \partial J_i \partial J_j$ . Note that if the frequencies are functions solely of the Hamiltonian (as in the Kepler case)  $\mathbf{n}$  is aligned with the stream particle frequency vectors and the stream is well approximated by an orbit. We will return to this point later in Section 3.4. Bovy (2014) and Sanders (2014) introduced a model for each tail of the stream (leading or trailing) in angle-frequency space that was an elongated Gaussian in the frequency offset from the progenitor and a isotropic Gaussian in initial angle offset from the progenitor. By estimating some stripping rate  $p(t)$  the angle-frequency distribution could be calculated at all times. Through the introduction of a linear transformation from position-velocity space to angle-frequency space in the neighbourhood of the stream, Bovy (2014) demonstrated that the

stream track in configuration space can be computed quickly and the model could be rapidly sampled at any time.

The angle-frequency model of a stream can be simply extended to include the effects of a gap. Under the assumption that the sub-halo imparts an instantaneous velocity kick to the stream particles, we can calculate the change to the angles and frequencies for small velocity kicks as

$$\begin{aligned} \delta\Omega^g &\approx \left. \frac{\partial \Omega}{\partial \mathbf{v}} \right|_x \cdot \delta\mathbf{v}, \\ \delta\theta^g &\approx \left. \frac{\partial \theta}{\partial \mathbf{v}} \right|_x \cdot \delta\mathbf{v}. \end{aligned} \quad (13)$$

This is a good approximation as the transformation between  $(\mathbf{x}, \mathbf{v})$  and  $(\Omega, \theta)$  is close to linear for the small velocity kicks from subhaloes. However, the assumption made here is not exactly the same as the impulse approximation of the previous section. Here we have

assumed the particle is fixed in the galactic frame whereas the impulse approximation assumes the particle is fixed in a frame moving at constant velocity  $\mathbf{v}$  with respect to the galactic frame. In practice, the difference between these assumptions does not produce a significant effect.

The stream stretches along the direction  $\mathbf{n}$  and in each tail the frequency distribution is very narrow such that, at a fixed time, the location of the particles in the stream are well approximated by a single angle coordinate  $\theta_{||} = \theta \cdot \mathbf{n}$ . We assume that the kicks are functions of this single variable. This assumption is equivalent to assuming the stream is very cold as we are ignoring any spatial extent of the stream perpendicular to the streaming direction. If the kick occurred a time  $t_g$  ago the angles and frequencies of a stream particle are given by

$$\begin{aligned}\Delta\theta &= \Delta\theta_{\text{init}} + \Delta\Omega_{\text{init}}(t_s - t_g) + \delta\theta^g + (\Delta\Omega_{\text{init}} + \delta\Omega^g)t_g \\ &= \Delta\theta_{\text{init}} + \Delta\Omega_{\text{init}}t_s + \delta\theta^g + \delta\Omega^g t_g, \\ \Delta\Omega &= \Delta\Omega_{\text{init}} + \delta\Omega^g.\end{aligned}\quad (14)$$

Note that these kicks are only valid if  $t_s > t_g$  i.e. the particle was in the stream at the kick time, otherwise the applied kicks to the angles and frequencies are zero. The particle moves with its initial frequency separation until the kick at which point the particle continues to move at the initial frequency separation plus the frequency kicks.

The matrices  $\left. \frac{\partial\theta}{\partial v} \right|_x$  and  $\left. \frac{\partial\Omega}{\partial v} \right|_x$  must be calculated numerically. However, we will demonstrate that there are several approximate analytic relations that hold well for the inspected simulation.

### 3 SIMULATION

We use two simulations to investigate the formation of stream gaps in actions, angles and frequencies. Here we describe the set-up of the simulations. The stream progenitor is a King profile globular cluster with  $W_0 = 5$ , a mass of  $10^5 M_\odot$  and a core radius of  $r_c = 13$  pc. The cluster was modelled with  $10^6$  particles and a smoothing length of 1 pc. The galactic potential was modelled as a logarithmic halo of the form in equation (9) with  $V_c = 220$  km s $^{-1}$  and  $q = 0.9$ . The cluster was placed on an eccentric orbit with a pericentre of 15 kpc and apocentre of 30 kpc, and the cluster was released around apocentre at (30, 0, 0) kpc with an initial velocity of (0, 105.75, 105.75) km s $^{-1}$ . Both simulations were run for 10 Gyr and the stream was then impacted with a Plummer subhalo of mass  $10^8 M_\odot$  and scale radius  $r_s = 625$  pc. The impact point was near pericentre with a impact parameter of  $b = 0$  and the velocity is perpendicular to the stream plane at this point with magnitude of 200 km s $^{-1}$ . The subhalo was inserted into the simulation 100 Myr before impact and removed 100 Myr after impact. The simulation was then evolved for a further 5 Gyr. The simulation was run using GADGET-3 (which is an improved version of GADGET-2, Springel 2005). In Figure 3 we show the full stream in the  $(x, y)$  plane and a zoom-in of the gap centre at 880 Myr after impact.

#### 3.1 Action, angle & frequency structure

Here we investigate the angle, action and frequency structure of the stream. We take the snapshot of the stream at 880 Myr after impact and compute the angles, frequencies and actions for all particles

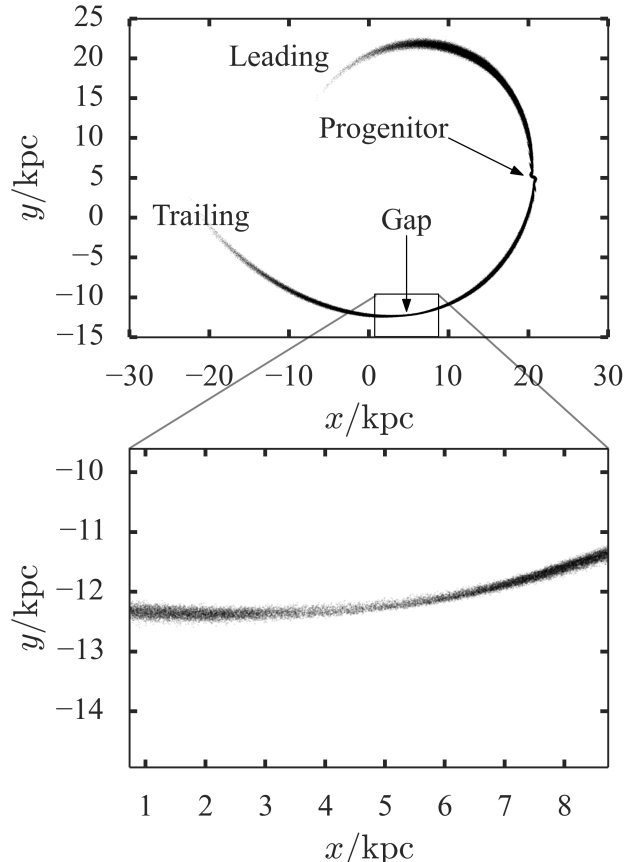


**Figure 3.** Real-space distribution of stream and gap zoom-in for the  $10^8 M_\odot$  subhalo fly-by.

in the trailing stream tail (defined by a spatial cut). We also perform the same calculation for the stream evolved without a subhalo flyby. In Fig. 4 we show histograms of the difference in the density in angle, frequency and action space between the perturbed and unperturbed simulation. We plot all quantities with respect to the coordinates of the gap centre which is defined by eye. In the angle and frequency distributions there is a clear under-density along the stream direction. In action space we also observe an under-density at the centre of the distributions but the exact geometry of the under and over-densities is complex and clearly depends on the nature of the stream track and subhalo properties. We will discuss this further later in Section 3.4.

In Figure 5 we plot the angles and frequencies for unperturbed and perturbed trailing stream distributions. The unperturbed simulation consists of a spur due to each stripping event. The material stripped in each event forms an approximately vertical line in this space before gradually twisting clockwise as the differential frequency effects take hold. The material on the far left was stripped earliest. We see that the subhalo produces the expected S-shape which also twists clockwise in time due to the differential frequency effects. At  $t = 0$  there is a clear gap in frequency but only a relatively modest gap in angle. However, the twisting produces a larger gap in the angles. The twisting also causes some perturbed material to overtake the unperturbed material.

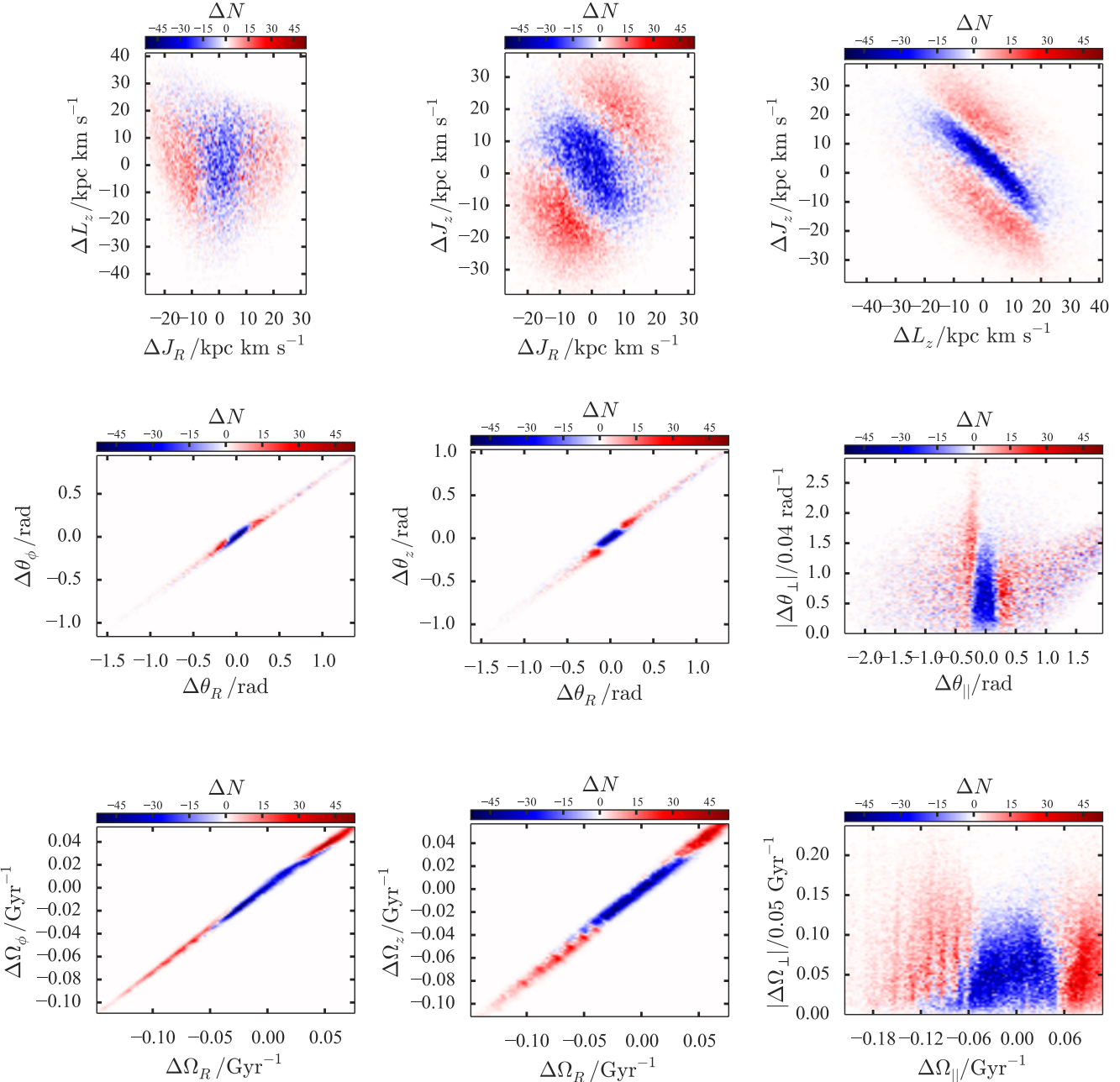


**Figure 4.** Difference histograms between the unperturbed and perturbed streams at  $t = 0.88$  Gyr: the top row shows the distribution in actions, middle row the angles and bottom row the frequencies. The right panels in the second and third rows show the distributions in the parallel-perpendicular space where ‘parallel’ is the distance along the stream direction and ‘perpendicular’ is the Euclidean distance from the stream direction vector. Zero-points correspond to the gap centre (defined by eye).

### 3.2 Kicks

In Section 2.2 we described how the angle and frequency kicks due to a subhalo can be computed under a linear approximation from the velocity kicks. Here we use the expressions and compare the resulting kicks with those measured from the simulation.

We begin by taking the snapshot of the unperturbed stream at the impact time and form a stream track by fitting a spline to the stream particles. We then compute the vector  $\mathbf{n}$  from this track and at each point along the stream track compute  $\theta_{||} = \theta \cdot \mathbf{n}$  as

well as  $\delta\Omega^g(\theta_{||})$  and  $\delta\theta^g(\theta_{||})$  by finite differencing in velocity at fixed position. We show the resultant kicks in Fig. 6. We also show the angle and frequency kicks computed from the simulation. In the case of the frequency kicks we simply difference the perturbed and unperturbed simulation. In the case of the angles we calculate the angles and frequencies of the perturbed simulation snapshot at  $t = 0.88$  Gyr and rewind to the impact point before differencing with the unperturbed snapshot. The frequency match is satisfactory whilst the angle kicks are perhaps less satisfying a match. This may be as we have rewound to  $t = 0$  whilst the angles still experience

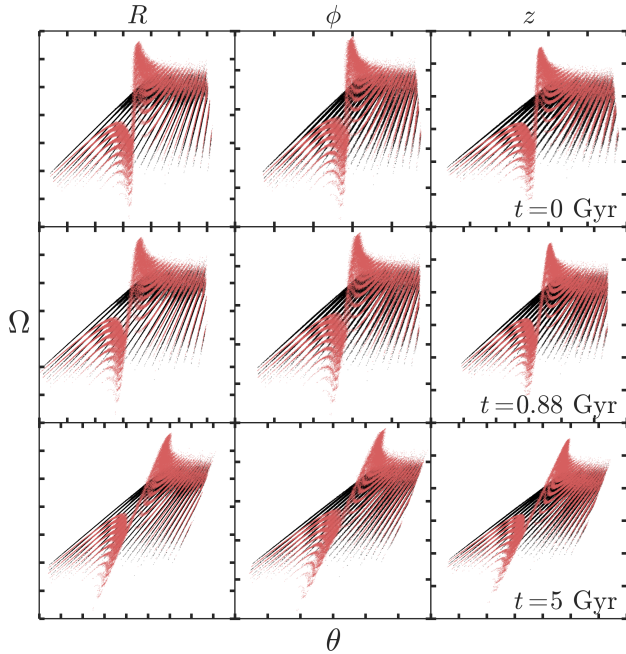


**Figure 5.** Frequency-angle distributions for unperturbed (black) and perturbed (red) trailing tail at three different times. Each row shows a different time written in the rightmost column. The three columns from left to right show the radial angle against radial frequency, the azimuthal angle against azimuthal frequency and vertical angle against vertical frequency.

a significant force for some time after this. However, it may also be due to the assumption of the impact approximation and the linear map i.e. the position of the particles are fixed during the fly-by. We performed several checks of the accuracy of the angle computation: we measured the fluctuations in the angle calculation about a straight line in angle space and also compared a snapshot evolved in angle-frequency space with a later simulation snapshot. These tests show that the angles are computed to an accuracy of  $\sim 10^{-3}$  rad such that the discrepancy observed here cannot be due to errors in the computation.

### 3.3 Model-simulation comparison

With the angle and frequency kicks satisfactorily calculated we proceed to take the unperturbed simulation, apply the kicks and compare with the perturbed simulation at later times.

In Fig. 7 we show the angle and frequency distributions of the unperturbed simulation, the perturbed simulation and our model constructed by perturbing the angles and frequencies of the unperturbed simulation for the stream after 880 Myr. The match is very good and there is a clear gap in both angle and frequency.

In Fig. 8 we plot the unperturbed and perturbed stream in angle space at four different times (0 Gyr, 0.88 Gyr, 3 Gyr and 5 Gyr after impact) along with the model constructed by perturbing the unperturbed stream with the impulse approximation. Additionally we show the difference between the perturbed and unperturbed angle distributions. We see at all times there is a gap in  $\theta_z$  and  $\theta_R$  with an overdensity at 0 Gyr after impact in  $\theta_\phi$ . The gap grows in time in all angles, and our model matches the distributions well at all times.

### 3.4 Analytic approximations

We now develop some understanding of the magnitude of the angle, frequency and action kicks by inspecting some cases where we can calculate these quantities analytically.

For scale-free potentials of the form  $\Phi \propto r^\alpha$  Williams et al. (2014) demonstrated that the Hamiltonian in action-space is well approximated by

$$H(\mathbf{J}) \propto (J_R + BL)^\beta, \quad (15)$$

where  $\beta = 2\alpha/(2 + \alpha)$ ,  $B$  is a constant and  $L$  is the angular momentum. They also suggest that in scale-free flattened axisymmetric potentials of the form  $\Phi \propto (R^2 + (z/q)^2)^{\alpha/2}$  the Hamiltonian is well approximated by

$$H(\mathbf{J}) \propto (J_R + BL_z + CJ_z)^\beta, \quad (16)$$

where  $B$  and  $C$  are constants. In these potentials the frequencies depend on the actions solely through the Hamiltonian as  $\Omega_i \propto H^{(\beta-1)/\beta}$  so we find that

$$\frac{\delta\Omega_i^g}{\Omega_i} = \frac{\beta-1}{\beta} \frac{\delta H}{H}. \quad (17)$$

Note in the case of the harmonic oscillator  $\beta = 1$  and the right-hand side vanishes as the frequencies are energy independent. This equation can also be derived when considering the change in the energy and hence azimuthal frequency of a circular orbit. The analogous approximate expression for the Hamiltonian in the scale-free logarithmic potential is

$$H(\mathbf{J}) = V_c^2 \log(J_R + BL_z + CJ_z)), \quad (18)$$

such that

$$\frac{\delta\Omega_i^g}{\Omega_i} = -\frac{\delta H}{V_c^2}. \quad (19)$$

In the case of a subhalo flyby  $\delta H^g = \mathbf{v} \cdot \delta\mathbf{v}^g$ . We plot this approximation for the simulated stream in Fig. 9.

We would like to find analogous expressions for the actions and angles. We approximate the changes in the actions as

$$\begin{aligned} \delta J_R^g &\approx \frac{\delta H^g - \Omega_\phi \delta L^g}{\Omega_R}, \\ \delta L_z^g &\approx (\mathbf{r} \times \delta\mathbf{v}^g)_z, \\ \delta J_z^g &\approx \frac{v_z \delta v_z^g}{\Omega_z}, \end{aligned} \quad (20)$$

where  $\delta L = \mathbf{L} \cdot \delta\mathbf{L}^g / |\mathbf{L}|$  the change in the angular momentum. The change in  $J_R$  comes from the spherical approximation and the change in  $J_z$  from the assumption that it is a harmonic oscillator in the  $z$  direction. We show these analytic approximations in Fig. 10 along with the kick distributions overlaid on the difference plots of Fig. 4. The analytic approximations recover the magnitude of the kicks within a factor of  $\sim 1.5$  but are not nearly as impressive as the frequency kick analytic expressions. These approximations work better for streams confined to the meridional plane. However, we see from the lower panels of Fig. 10 that the correlations between the action kicks are well recovered and explain the observed structure in the action difference plots. Note that our unperturbed stream model is a function of the angles and frequencies such that the action kicks are unimportant for modelling purposes.

Finally, we turn to the angle coordinates. From our investigations there do not appear to be any particularly neat or understandable analytic expressions we can derive for these quantities. What follows are some loose arguments to get a handle on the amplitude of the angle kicks relative to the frequency kicks. We inspect

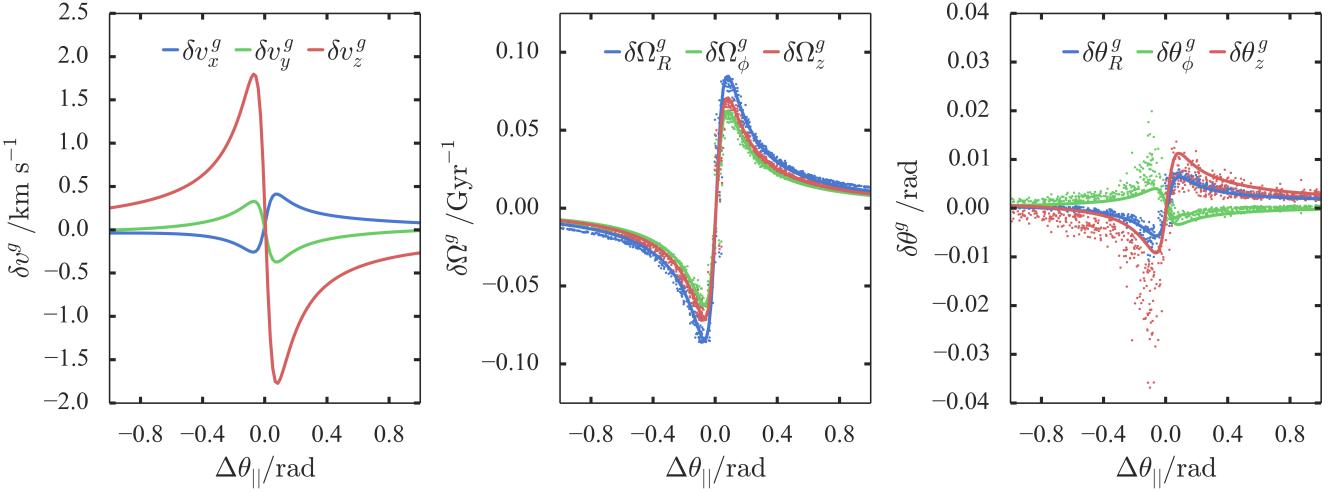


**Figure 6.** Angle and frequency kicks: the points are a random sample of 1000 particles from the stream and show the kicks found from the simulations whilst the lines show those calculated under the impulse approximation.

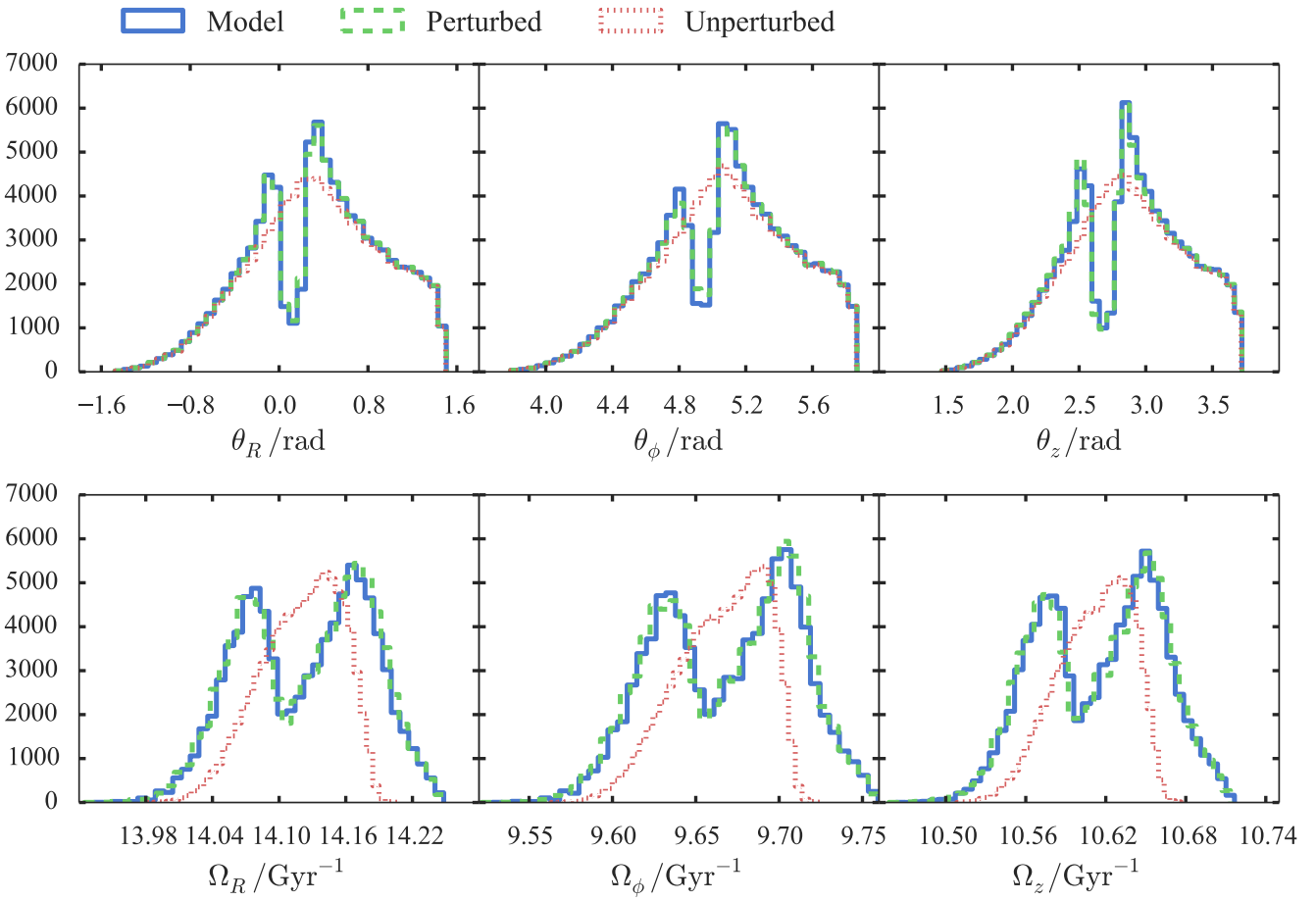


**Figure 7.** Angle and frequency distributions for the perturbed and unperturbed stream model: the red histograms show the unperturbed stream  $t = 0.88$  Gyr after impact, the green show the perturbed stream and the blue show the unperturbed stream kicked in angle and frequency space and evolved to the current time.

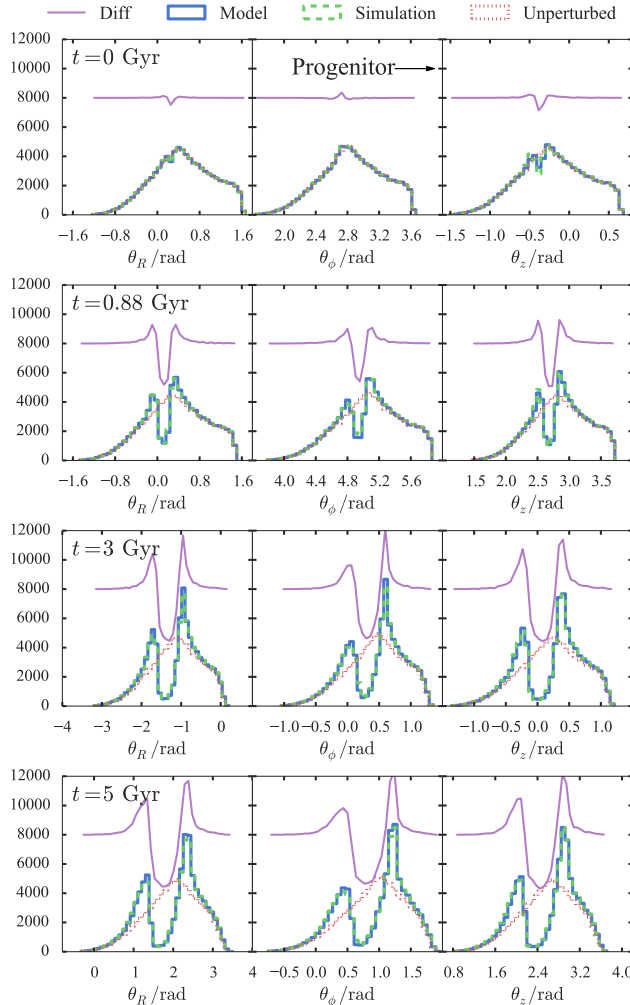


**Figure 8.** Unperturbed, perturbed and model stream: the red histograms show the unperturbed stream, the green show the perturbed stream and the blue show the unperturbed stream kicked in angle and frequency space and evolved. The purple line shows the difference between the perturbed and unperturbed streams offset by some arbitrary amount. The four rows show 0, 0.88, 3 and 5 Gyr after impact.

the harmonic oscillator (which is also appropriate for small oscillations about a circular orbit and perpendicular to the plane). The angle coordinate  $\theta_i$  is given by

$$\tan \theta_i = \frac{\Omega_i x_i}{v_i}, \quad (21)$$

where  $x_i$  is the position coordinate relative to the minimum,  $v_i$  is the velocity coordinate. For the angle kicks we find that

$$\delta\theta_i^g \approx \frac{\tan \theta_i}{1 + \tan^2 \theta_i} \left( \frac{\delta\Omega_i^g}{\Omega_i} - \frac{\delta v_i}{v_i} \right), \quad (22)$$

For a true harmonic oscillator the change in frequency is identically zero such that this expression can be reduced to

$$\delta\theta_i^g \approx -\frac{\delta v_i}{\sqrt{E}} \sin \theta_i = -\frac{1}{2} \frac{\delta v_i}{v_i} \sin 2\theta_i, \quad (23)$$

where  $E$  is the energy of the oscillation. We see that near a turning point ( $v_i \approx 0$ ) the angle kicks are largest and of order  $\delta v_i / \sqrt{E}$  and near the midpoints ( $x_i \approx 0$ ) the angle kicks are approximately zero.

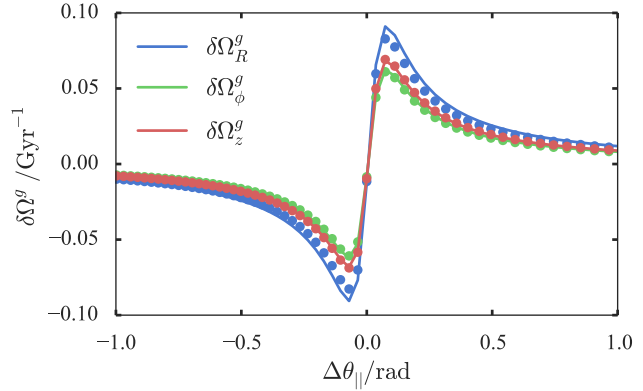


**Figure 9.** Analytic frequency kick approximation. The lines show the analytic relationship for the flattened logarithmic potential from equation (19) and the dots show the numerical calculation.

As expected the magnitude of the angle kicks are phase-dependent. Using equation (19) we see that

$$\frac{\delta\theta_i^g}{\delta\Omega_i^g} \approx \Omega_i^{-1} \left( \frac{V_c}{|\mathbf{v}_i|} \right)^2 \sin 2\theta_i, \quad (24)$$

where we have neglected geometric factors. The final two terms are of order unity such that these rather loose arguments convince us that this ratio is approximately the period of the oscillation in dimension  $i$ . From inspection of Fig. 6 we see that the ratio of the angle to frequency kicks is of order 0.1 Gyr which corresponds approximately to  $1/\Omega$  as  $\Omega_i \approx 10 \text{ Gyr}^{-1}$ . From inspection of the numerical results it appears  $|\delta\theta_i^g| \approx \delta\Omega_i^g / \Omega_i$  within factors of 3 for  $|\Delta\theta_||| < 1 \text{ rad}$ . Therefore, we have ascertained that the angle kicks are dominated by the frequency kicks after approximately one period.

### 3.5 Stages of stream growth

Erkal & Belokurov (2015a) discussed the three phases of stream gap formation in the limit that the stream itself is on a circular orbit. They found that on short time-scales (less than a radial period) an overdensity formed as the particles were scattered onto epicyclic orbits that brought them towards the gap centre. This was dubbed the compression phase. After approximately a radial period the stream enters an expansion phase where the gap begins growing until the perturbed material starts to overtake unperturbed material and caustics form. During the expansion phase the stream gap grows linearly in time whilst during the caustic phase the growth rate slows to  $t^{1/2}$ . In this section we investigate and discuss how this picture relates to the formalism presented here.

In Fig. 11 we plot the size of the gap in parallel angles as a function of time for the simulated stream. This is defined as the difference between the parallel angles of the points where the perturbed and unperturbed densities are equal. We produce a smooth difference histogram using kernel density estimation with a bandwidth of  $b = 0.04 \text{ rad Gyr}^{-1} t + 0.01 \text{ rad}$  for  $t < 1 \text{ Gyr}$  and  $0.05 \text{ rad}$  otherwise and then fit a spline to the resulting distribution (we use this smoothing kernel for all future results on the gap size and minimum/maximum densities in the stream with an additional factor in the bandwidth of  $0.5 \log_{10} M - 3$ ). We also show a best-fit power-law line ( $\Delta\theta_|| \propto t^{0.58}$ ) for the segment  $t < 5 \text{ Gyr}$  as well as the time-scales for the different stages of gap growth. The

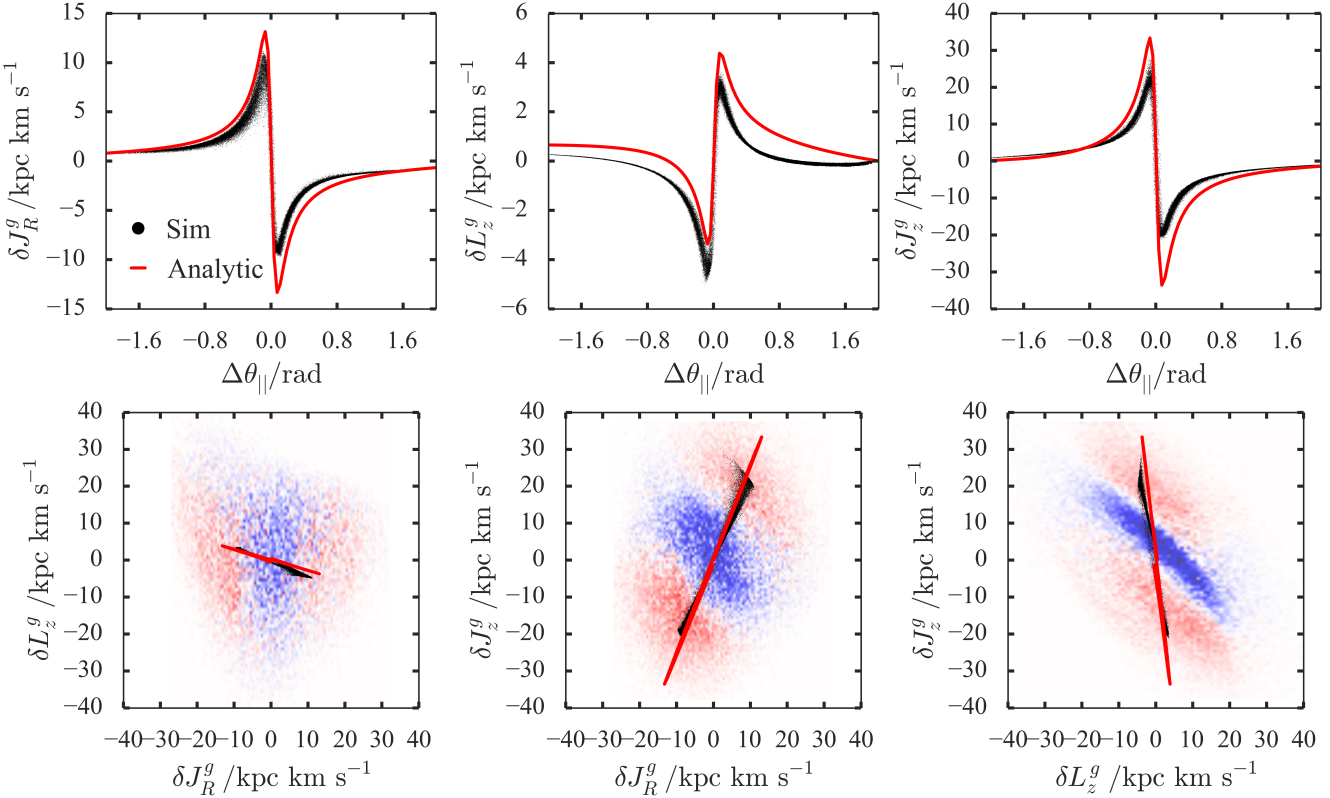


**Figure 10.** Analytic action kick approximation. In the top panels the red shows the approximate analytic expressions from equation (20) and the black is computed from the simulations. In the bottom panels we overlay the action kick distributions on the difference plots from Fig. 4. Clearly the analytic approximation explains the correlations observed in the simulation.

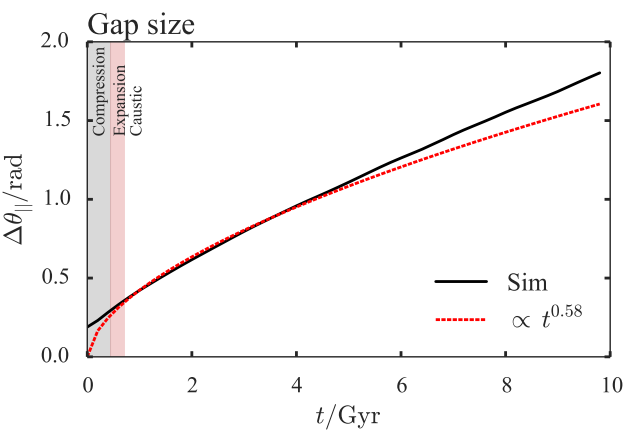


**Figure 11.** Gap size in parallel angle as a function of time. The black line shows the gap measured from the simulation and the dashed red line shows the best fitting power-law line for  $t < 5$  Gyr. We also mark on the three phases of the gap growth from Erkal & Belokurov (2015a).

compression phase lasts for a single radial period. The time-scale on which the caustic becomes important is computed from equation (26) of Erkal & Belokurov (2015a). In this example the expansion phase only lasts for  $\sim 200$  Myr but lowering the subhalo mass to  $10^7 M_\odot$  increases its length to  $\sim 600$  Myr. We note that there is a gap in parallel angle at  $t = 0$ . This does not correspond to a spatial

gap but is due to the angle kicks from the subhalo that have shifted the stars to slightly different orbital phases. It is intriguing that the size of the initial gap in parallel angles is significantly larger than the peak of the angle kicks shown in Fig. 6. However, one must consider the collective effects of a series of particles being kicked in order to compute the gap size. For instance, if the unperturbed parallel angle distribution  $N_0(\theta_{||})$  were a uniform distribution the perturbed distribution  $N(\theta_{||})$  would be given by

$$N(\theta_{||}) = \int d\theta'_{||} N_0(\theta'_{||}) \delta(\theta_{||} - \theta'_{||} - \delta\theta_{||}^g(\theta'_{||})) \propto (1 + \frac{\partial \delta\theta_{||}^g}{\partial \theta_{||}})^{-1}. \quad (25)$$

The gap size is then related to the zeros of

$$\frac{\partial \delta\theta_{||}^g}{\partial \theta_{||}}$$

and the peaks in the perturbed distribution are at the zeros of the second derivative

$$\frac{\partial^2 \delta\theta_{||}^g}{\partial \theta_{||}^2}.$$

In Fig. 12 we show the second derivative computed for our example as well as the quantity

$$(1 + \frac{\partial \delta\theta_{||}^g}{\partial \theta_{||}})^{-1} - 1. \quad (26)$$

The second derivative is zero around  $\delta\theta_{||} \approx 0.16$  and equation (26) crosses zero around  $\delta\theta_{||} \approx 0.1$ . These correspond well

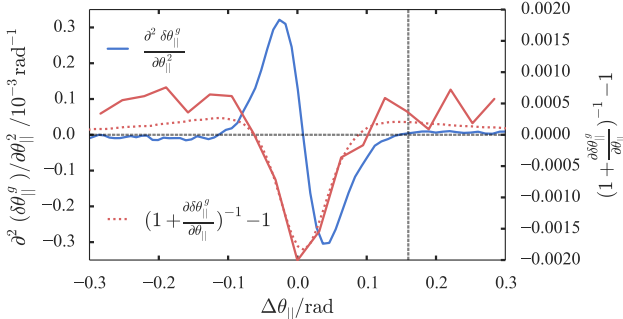


**Figure 12.** Derivatives of the parallel angle kicks: the solid blue line shows the second derivative of the kicks whilst the dotted red line shows the expression from equation (26). The solid red line shows the scaled density contrast from the simulation. The black lines show the zero line and the approximate location of the peak density contrast.

to the observed initial amplitude of the parallel-angle gap size ( $\sim 0.2$ ). We also show the density contrast computed from the simulations which correlates well with equation (26). As the angle kick depends upon  $\theta_{||}$  and is larger at small  $\Delta\theta_{||}$  and the range of  $\Delta\theta_{||}$  over which the kicks are important is larger than the angle kicks (see Fig. 7), the gap that forms is larger than perhaps expected. If the angle kicks were large compared to the range in  $\Delta\theta_{||}$  over which the kicks are important the gap size would be approximately the amplitude of the angle kicks. Therefore, we conclude that there is not a one-to-one correspondence between the amplitude of the angle kicks and the initial parallel angle gap size, and the latter can be significantly greater than the former.

The initial angle kick appears to dominate on a time-scale of  $\sim 400$  Myr after which the best-fit power-law is a much better match. This also appears to correlate with the end of the compression phase. Therefore, it seems that the compression phase is associated with the initial angle kicks. We can understand this by considering a simple example of a stream on a radial orbit. Here the parallel angle is purely the radial angle. The shape of the angle kicks will be very similar to those in Fig. 6 with the particles in front of the gap given a positive kick and those behind given a negative kick. At a fixed position increasing the radial angle means we are now closer to apocentre so the apocentre has moved inwards and the particle must move more slowly. Likewise decreasing the radial angle moves apocentre further out and the particle must move faster. Therefore, the particles behind the gap move faster than those in front and an overdensity forms.

We use the formulae from Erkal & Belokurov (2015a) to calculate the time-scale on which the caustic begins to form. In this case the expansion phase is very short and so the subsequent evolution should go with the square-root of time. We see, however, that this is only approximately true up to  $\sim 4$  Gyr (the best-fitting power law is  $t^{0.58}$ ) after which the growth rate is faster than this. We will return to this point later in Section 4 and only mention here that it is due to the gap forming on an already growing underlying stream.

Our discussion has related to the size of the gap in parallel angle. Whilst this is an appropriate space for understanding general stream morphology it is awkward to see the relationship with the observed stream properties. We briefly investigate this by projecting the model back into real-space. For this purpose we use the publicly-available torus code from McMillan, Binney & Dehnen

(2015, in prep.). We construct eight tori on the corners of an action-space box that encompasses the full perturbed distributions and interpolate the frequencies to find the actions of the perturbed particles. We then interpolate the Fourier coefficients of the tori in action-space to construct a torus of the required actions for each particle and request the  $(x, v)$  corresponding to the angles of the particle. We then find a plane that minimises the perpendicular spread of the stream and compute the size of the gap in the azimuthal angle in the plane in the same way as in parallel angle space. We plot both the azimuthal gap size and the parallel angle gap size as a function of time in Fig. 13. As expected the azimuthal gap size oscillates but it is well enveloped by the parallel angle gap size and it appears that the average azimuthal gap size correlates well with the parallel angle gap size. We note that the amplitude of the oscillations of the azimuthal gap size can be estimated by considering conservation of angular momentum. If two particles in the stream had identical angular momentum their azimuthal separation  $\Delta\phi \sim r^{-2}$  resulting in a gap size which varies by a factor of  $(r_{\max}/r_{\min})^2$  over the orbit. For our simulation means the azimuthal separation fluctuates by a factor  $\sim 4$ , which agrees well with Fig. 13. We also can clearly see the gap forms immediately in parallel angle whilst in azimuthal angle there is a small peak due to the compression phase.

We also plot the minimum and maximum density contrasts (defined as perturbed divided by unperturbed density). The azimuthal density contrast oscillates about the parallel angle density contrast, and both plateau at late times ( $t > 4$  Gyr). Erkal & Belokurov (2015a) showed that the minimum density contrast falls as  $1/t$  at large times, and the maximum grows as  $t$  at small times and like  $1/(1 - at)$  at large times with caustics forming at  $t = 1/a$ . These properties are well reproduced by our simulation. Continuing the approximate modelling of equation (25) and including the assumption that the particles all move at the same frequency we find that the density contrast at later times is proportional to

$$(1 + \frac{\partial\delta\Omega_{||}^g}{\partial\theta_{||}}t)^{-1} - 1. \quad (27)$$

This expression is much like those derived by Erkal & Belokurov (2015a) in the circular-orbit limit. For a uniform unperturbed angle distribution the minimum density contrast occurs at  $\Delta\theta_{||} = 0$  and so falls as  $1/(1 + Ct)$  where  $C$  is a constant. The maximum density occurs when the bracket diverges such that the caustic behaviour of Erkal & Belokurov (2015a) is recovered. We note that in reality the minimum density contrast in Fig. 13 falls more slowly than  $1/t$  at large times and actually reaches a constant. This is due to the spread of frequencies/energies in the stream. Similarly the spread in energies in the stream gives rise to the finite peak observed in the density contrast.

#### 4 VARYING THE IMPACT PROPERTIES

We have demonstrated that we are able to adequately model the impact of a subhalo on a stream and the subsequent evolution. With this machinery in place we are able to rapidly simulate the effects of any subhalo fly-by. In this section we will discuss the differences in the subsequent stream structure as a function of the subhalo mass and the subhalo impact location. We repeat the exercise performed in Section 3 of simulating the subhalo fly-by on a simulated unperturbed stream and inspecting the subsequent evolution.

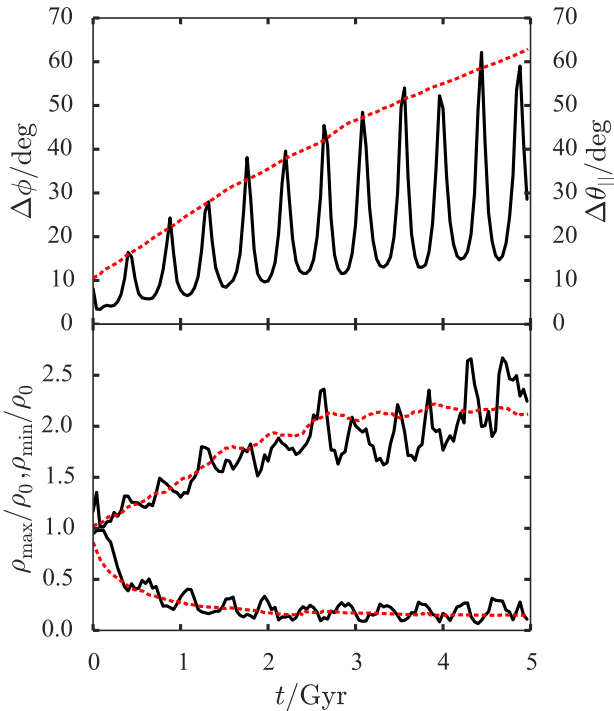


**Figure 13.** Gap properties in real and angle space. In the top panel we show the gap size in the azimuthal angle of a plane fitted through the stream in solid black and the gap size in parallel angle in dashed red. In the bottom panel we show the minimum and maximum density contrast in these two spaces.

#### 4.1 Varying the subhalo mass

First, we investigate the properties of the stream as a function of subhalo mass. We adopt the scaling relation between the mass and scale radius of the subhalo Plummer sphere of

$$M \propto r_s^{2.5}, \quad (28)$$

which roughly matches the scaling between mass and scale radius in Via Lactea II (Diemand et al. 2008). Keeping all other properties of the subhalo fly-by the same we simulate the effects of a  $10^7 M_\odot$  and  $10^{7.5} M_\odot$  subhalo. In Figure 14 we show the gap profile after  $t = 880$  Myr, the gap size as a function of time and the minimum and maximum density contrast as a function of time. As expected the gap size is deepest and grows fastest for the highest mass subhalo. In all cases the minimum density contrast plateaus in time and the value that the density contrast plateaus to decreases with mass. As shown in Erkal & Belokurov (2015a) the amplitude of the velocity kicks scales as  $(M/r_s)$  and the spatial gradients of the velocity kicks around the point of closest approach also scale with this quantity. From the approximate relation of equation (3.4) we find that both the amplitude of the frequency kicks and the gradient of the frequency kicks with the parallel angle at the gap centre also scale with this quantity. Therefore, it naturally follows from equation (27) that at large times  $\rho_{\min}/\rho_0 \sim (M/r_s)^{-1} \sim M^{-0.6}$  such that there is a factor 4 difference in depth between the  $10^8 M_\odot$  and  $10^7 M_\odot$  cases which is observed in Fig. 14.

#### 4.2 Varying the impact geometry

Now we investigate how the stream changes as a function of where along the stream the impact occurs. In addition to the inspected geometry of Section 3 we simulate two other impacts at varying distance from the progenitor as shown in the top left panel of Figure 15. The impact close to the progenitor occurs at  $([x, y, z] = [-15.3, -9.8, 9.3] \text{ kpc}, [v_x, v_y, v_z] = [41.9, -183.0, 152.2] \text{ km s}^{-1})$  and the one further from the progenitor at  $([x, y, z] = [-1.2, 12.9, -10.8] \text{ kpc}, [v_x, v_y, v_z] = [-239.8, -100.6, 87.0] \text{ km s}^{-1})$ . Again, we fix all other parameters of the impact to those in the original simulation, including the absolute velocity of the subhalo (note that fixing the relative velocity between the subhalo and impact point in the stream does not change the conclusions drawn here). The near impact is in the regime where the mean parallel frequency is approximately constant with the parallel angle whilst the far impact is in the regime where the mean frequency is decreasing linearly with the parallel angle. In this far regime the stream is well ordered in energies, whilst in the near regime the stream particles have not had sufficient time to order themselves by energy. We plot the difference between the perturbed and unperturbed simulations in parallel angle for two times. The density contrast at the large negative parallel angle for the far case is very large at late times as the number density in the unperturbed simulation at these large separations is low. A similar effect is seen at large positive parallel angle for the near case but here it should be noted that we have not included the effect of more stars entering the stream as they are stripped from the progenitor. In the lower panels we show the gap size and the minimum/maximum density contrast as a function of time. The gap size in all three cases is very similar for  $t < 3$  Gyr but they diverge at larger times as the far impact gap size increases faster than the near impact. We can understand this as in the far case the gap is forming on an already growing stream as the underlying stream structure is well ordered. However, in the near case the stream is mixed so the underlying stream is growing more slowly. In all cases the minimum density plateaus to a similar value. Note that we have shown two lines for the maximum density contrast for the two peaks on either side of the gap. In both the far and near cases one of the peaks diverges rapidly and correlates with the observations in the middle panels.

### 5 A FULL GENERATIVE PERTURBED STREAM MODEL

Up until now we have used a simulation as our unperturbed stream model to which we have applied the kicks. We now produce a full model of the perturbed stream that starts from a model for the unperturbed stream. For the latter, we use the model presented in both Bovy (2014) and Sanders (2014). This model is a fully generative model that models the expected stream structure in angle-frequency space with simple analytic distributions and projects this structure into the space of observables. In angle-frequency space a model is expressed in full generality as

$$\begin{aligned} p(\Omega, \theta, t_s) = \\ p(\Delta\theta_{\text{init}} = \Delta\theta - \Delta\Omega t_s) | \Omega_{\text{init}}, t_s) p(\Delta\Omega_{\text{init}} = \Delta\Omega | t_s) p(t_s). \end{aligned} \quad (29)$$

(see equation (12)). The specific model investigated by Bovy (2014) and Sanders (2014) simplified this to

$$p(\Omega, \theta, t_s) = p(\Delta\Omega_{\text{init}}) p(\Delta\theta_{\text{init}}) p(t_s), \quad (30)$$

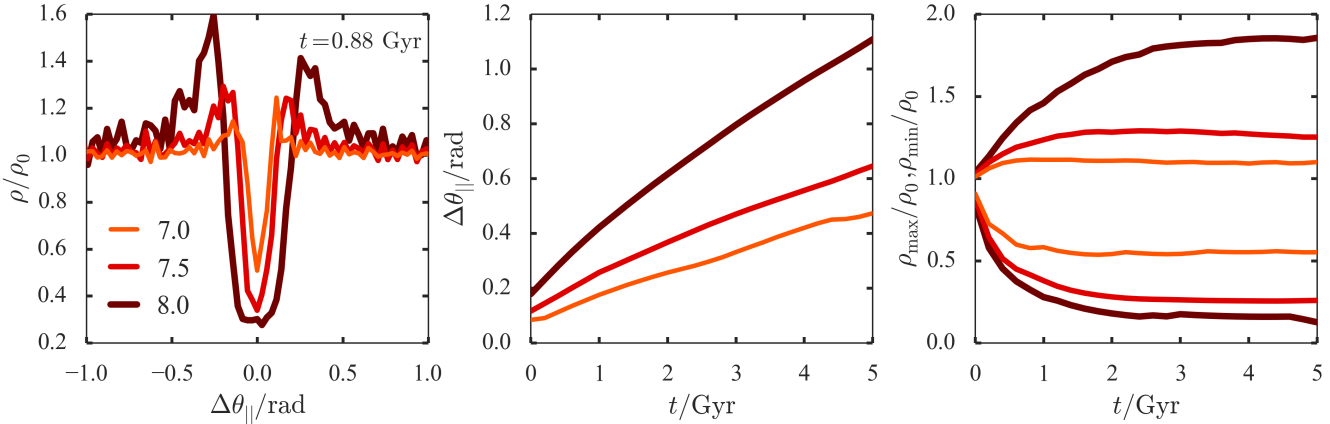


**Figure 14.** Properties of the stream as a function of subhalo mass. The thick brown line corresponds to  $10^8 M_\odot$ , the medium red line  $10^{7.5} M_\odot$  and the thin orange line  $10^7 M_\odot$ . The left panel shows the difference between the perturbed and unperturbed simulations in parallel angle after  $t = 880$  Myr, the middle panel shows the gap size as a function of time and the right panel shows the minimum and maximum density contrast as a function of time.

by assuming that the distribution of frequency offsets  $\Delta\Omega_{\text{init}}$  and angle offsets  $\Delta\theta_{\text{init}}$  is independent of stripping time  $t_s$ . In Section 5.1 we discuss how this is *not* a good assumption for the simulated stream considered in this paper and how we modify the model to account for this. However, a simple model of the form in equation (30) is still useful, as it allows the location of the stream in frequency–angle and configuration space to be efficiently calculated, both at the present time and at the time of impact.

In the model of Bovy (2014) and Sanders (2014),  $p(\Delta\Omega_{\text{init}})$  is a bimodal distribution, because there are peaks at positive and negative  $\Delta\Omega_{\text{init}}$  corresponding to the leading and trailing tails. Here we focus on modelling the trailing tail so we only consider negative  $\Delta\Omega_{\text{init}}$ . The distribution  $p(\Delta\Omega_{\text{init}})$  is chosen to be as in Bovy (2014). This distribution is approximately Gaussian with axes that approximately align with the eigenvalues of the Hessian matrix  $D_{ij} = \partial^2 H / \partial J_i \partial J_j$ . The angle distribution  $p(\Delta\theta_{\text{init}})$  is a simple isotropic Gaussian. In the simplest model, the stripping rate  $p(t_s)$  is taken as a uniform distribution up to some maximum time  $t_d$ —the disruption time—in Bovy (2014). For the uniform stripping rate, the location of the mean stream track in frequency–angle space can be computed analytically. To compute the transformation from angles and frequencies to Galactocentric Cartesian coordinates we interpolate the linear transformation computed for a series of points along the stream track as described in Bovy (2014).

The model for the perturbed stream can be obtained from the model of the unperturbed stream by computing the kicks at the time of impact and applying these as in equation (14). To compute the kicks we approximate the stream as being one dimensional along  $\theta_{||}$  with a point of closest approach  $\theta_{||,c}$ , which is a model parameter. We use the same method as discussed in Section 4.2 of Bovy (2014) to compute the mean stream track  $(\mathbf{x}, \mathbf{v})(\theta_{||})$  and the derivatives  $\frac{\partial \mathbf{x}}{\partial v}(\theta_{||})$  and  $\frac{\partial \mathbf{v}}{\partial v}(\theta_{||})$  along the track. Then we compute the velocity perturbation  $\delta \mathbf{v}(\theta_{||})$  due to the subhalo along the track and propagate it to the kicks in  $\delta\Omega^g(\theta_{||})$  and  $\delta\theta^g(\theta_{||})$  as in equation (13).

From this model we can generate mock streams by sampling a stripping time  $t_s$ , an initial frequency separation  $\Delta\Omega_{\text{init}}$  and an initial angle separation  $\Delta\theta_{\text{init}}$  from the unperturbed model. We then perturb them with  $\delta\Omega^g$  and  $\delta\theta^g$  based on their  $\theta_{||}$  at the time of impact. With these chosen, the current angles and frequencies are

known (see equation (14)) and hence the observables can be computed.

We set the velocity-dispersion parameter of the model by scaling that obtained in Bovy (2014) for a similar, but lower mass, stream. As shown in Sanders & Binney (2013a) for instance the properties of the stream in angles and frequencies scales with the mass of the progenitor,  $M$ , as  $M^{1/3}$ .

## 5.1 Modifications to model

We found that the simple model described above did not completely describe the simulation (in particular the density along the stream near the gap) such that several modifications are necessary. Firstly, the stream distribution in  $\Omega_{||}$  is not well described by a Gaussian, but instead is better fitted by two Gaussians. Inspection of the stream distribution in  $\Delta\Omega_{||}$  and  $\Delta\theta_{||}$  shows that the stream consists of material stripped in two separate ways:  $\sim 72$  per cent of the material is stripped around pericentric passage and this material forms a broad peak in  $\Delta\Omega_{||}$  that is separated from the progenitor by  $\mu_{\text{peri}} = 0.31 \text{ Gyr}^{-1}$  with a width of  $\sigma_{\text{peri}} = 0.05 \text{ Gyr}^{-1}$ . The other  $\sim 28$  per cent material is more continuously stripped, or evaporates, from the progenitor. This material forms a narrower peak in  $\Delta\Omega_{||}$  that is less separated from the progenitor at  $\mu_{\text{evap}} = 0.25 \text{ Gyr}^{-1}$  with a width of  $\sigma_{\text{evap}} = 0.023 \text{ Gyr}^{-1}$ .

Additionally, inspecting the distribution of  $\Delta\theta_{||}/\Delta\Omega_{||} \approx t_s$  showed that the stripping time (averaged over a time longer than an orbital period of the progenitor) is not uniform in time, but instead decreases slowly over time, such that a particle is more likely to have been stripped long ago. We modelled this by making  $p(t_s) \propto t_s$  for both the periodic stripping and for the more steady evaporation. In conclusion, compared to the simple model above, the distribution  $p(\Delta\Omega_{||}, t_s)$  cannot be separated as  $p(\Delta\Omega_{||}) p(t_s)$  in this model and the distribution of parallel frequency separation and stripping time looks like

$$\begin{aligned}
 p(\Delta\Omega_{||}, t_s) \propto & (1 - w)t_s \mathcal{N}(\Delta\Omega_{||} | \mu_{\text{peri}}, \sigma_{\text{peri}}) \\
 & \times \sum_n^{\text{int}([t_d - t_R]/T_R)} \delta(t_s - nT_R - t_R) \\
 & + wt_s \mathcal{N}(\Delta\Omega_{||} | \mu_{\text{evap}}, \sigma_{\text{evap}}),
 \end{aligned} \tag{31}$$

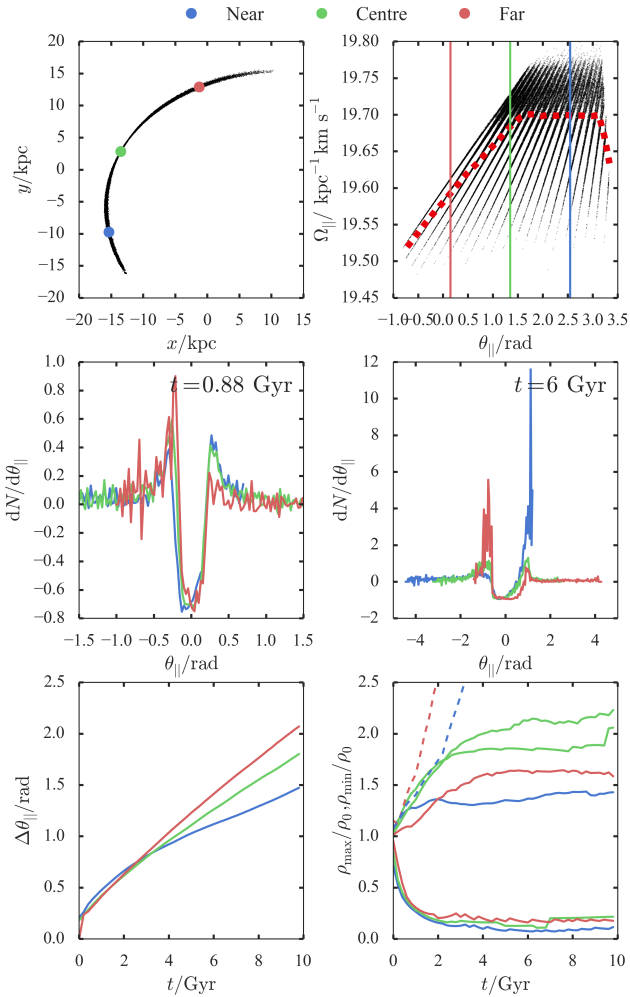


**Figure 15.** Properties of the stream as a function of the location of the impact point. **Top row:** The top left panel shows the stream in the  $(x, y)$  plane along with three dots showing the different impact points. The top right panel shows the location of these strikes in parallel angle as well as the distribution of the stream in parallel frequencies and angles. **Middle row:** The middle two panels show the relative density contrast  $\rho_{\text{perturbed}}/\rho_{\text{unperturbed}} - 1$  in parallel angle space for two separate times. **Bottom row:** The bottom two panels show the gap size in parallel angle and the minimum and maximum density contrast as a function of time with the dashed lines showing the divergent peak at low unperturbed density.

where  $\mathcal{N}(X|\mu, \sigma)$  is a Gaussian distribution with mean  $\mu$  and width  $\sigma$ .  $w = 0.28$  is the weight,  $T_R$  is the radial period,  $t_R$  is the time since last pericentric passage and  $\delta(t_s - nT_R - t_R)$  is a delta function expressing stripping at each pericenter passage.

We use this modified model to generate mock stream particles. To compute the impact kicks in this model as a function of  $\theta_{||}$ , we use the stream track at the time of impact computed in the simple model with the uniform distribution of stripping times discussed in the previous section. This is because the mean track cannot be computed easily for the non-separable  $p(\Delta\Omega_{||}, t_s)$  distribution, but can be estimated using the uniform  $p(t_s)$ , as  $p(t_s)$  mainly affects the density along the stream, but not its average location.

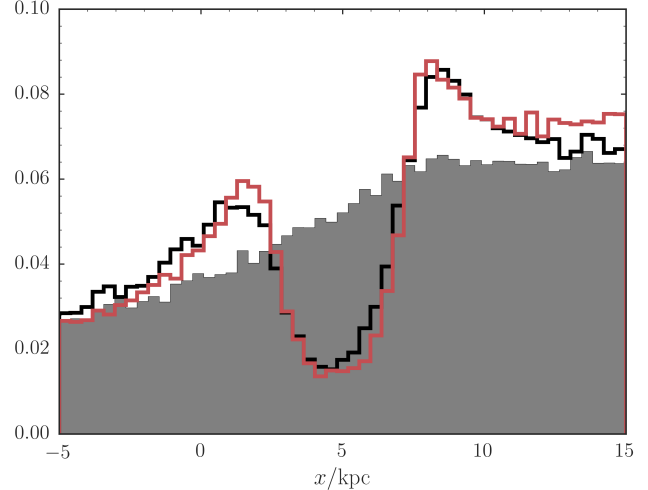


**Figure 16.** Density in a mock stream generated from the generative model described in the text (red) compared to that in the simulation (black) near the gap. The density of the unperturbed simulation is displayed in gray. The density in the simulation is well matched in the generative model.

## 5.2 Comparison to the simulation

We generate 100,000 mock stream particles from the generative model for the  $M = 10^8 M_\odot$  impact. The density along the stream in the simulation and of the mock stream is displayed in Figure 16. The gray, filled histogram shows the stream density in the unperturbed simulation for comparison. It is clear that the simple generative model provides an excellent match to the density in and near the gap in the simulation.

The simulated stream in configuration space near the gap is compared to the mock stream in Figure 17. The mock stream very closely follows the simulated stream. The bottom of each panel shows the difference between the phase-space coordinates in the perturbed and unperturbed simulation (black) and in the perturbed and unperturbed mock stream (red). These are computed by comparing the present coordinates of the same simulated/mock particles evolved with and without perturbation. That is, the perturbed and unperturbed simulation start from the same exact initial conditions and we do the same for the mock stream. It is clear from these bottom panels in Figure 17 that the perturbation due to the subhalo impact is very well described by the generative model described in this section.

## 6 CONCLUSIONS

We have presented a framework for modelling the formation of gaps due to the perturbation of a dark matter halo on a cold thin stream formed from progenitors on eccentric orbits. The formalism uses the simple description of dynamics provided by the action, angle and frequency coordinates. Stream particles obey simple equations of motion in this space which can be altered to incorporate the effects of a dark matter subhalo fly-by. An unperturbed stream is stretched along a single direction, described by the parallel angle coordinate, in which a gap forms when the stream is impacted by a subhalo.

We presented a simulation of a cold stream formed from a progenitor on an eccentric orbit in a scale-free flattened axisymmetric

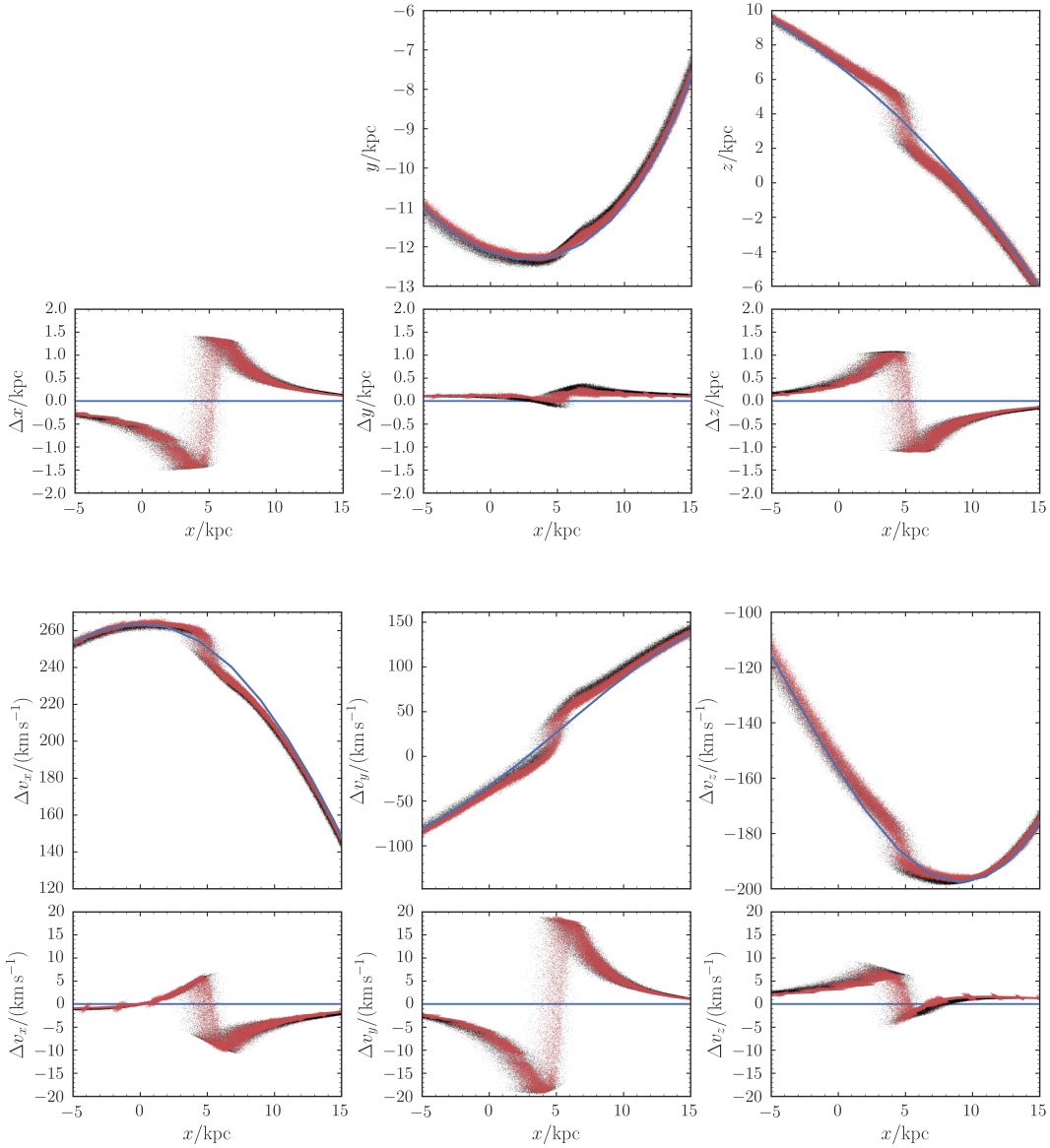


**Figure 17.** Comparison of the simulated stream (black) and the mock stream from the generative model (red) in configuration space. The bottom of each panel compares the difference in the phase–space position of each particle due to the subhalo perturbation in the simulation and the mock stream. The overall structure of the stream and in particular the phase–space offsets due to the subhalo perturbation are successfully modelled in the mock stream.

logarithmic potential. The stream was impacted by a  $10^8 M_\odot$  dark-matter subhalo and a gap formed in the stream. We analysed the formation of the gap in angle-frequency space and showed how the stream at all future times could be modelled using our framework. We found that generically the angle perturbation due to a fly-by is only important on time-scales less than a radial period. At later times the frequency perturbations are much more important and are simply related to the velocity perturbations in scale-free potentials such that the structure of the gap at late times is controlled by  $\mathbf{v} \cdot \delta\mathbf{v}^g$ .

We computed how the gap forms in the parallel angle (the angle along the stream) and showed that the distribution in this space can be simply related to the real-space properties of the gap. The evolution of the gap in angle-frequency space can be understood in the framework presented by Erkal & Belokurov (2015a).

We closed by showing how the structure of the gap varies as a function of the mass of the subhalo and the location along the stream the impact occurs. We found that, as expected, the parallel angle gap grows more slowly in time for lower mass subhaloes. The density contrast of the gap minimum plateaus to a constant value after a few Gyr for all inspected subhalo masses but the depth of this plateau increases with mass. The more interesting result is that the growth rate of the gap depends on the location along the stream where the impact occurs. We found that near the progenitor where the particles are mixed in energy the gap grows more slowly than far from the progenitor where the particles are well ordered in energy and so the gap forms on an already growing stream.

Whilst an underdensity in a stream is indicative of a subhalo fly-by, subhalo interactions are not the only cause of structure in a stream. Küpper et al. (2010) have shown that overdensities natu-

rally form in an eccentric stream due to epicyclic oscillations. This effect is incorporated in the angle-frequency models. Additionally, stream stars are not stripped at a constant rate but mostly stripped around pericentric passage and during disc passage. This naturally produces substructure in the stream nearest the progenitor where the particles have yet to order in energy. In the models presented in Bovy (2014) and Sanders (2014) the stripping rate was assumed constant. This was sufficient for modelling the full stream but when attempting to find and quantify substructure a clear handle on the stripping rate is necessary. Fortunately for a long stream that has gone through many stripping events the stripping rate should be quantifiable due to its anticipated periodicity. However, it becomes more difficult when dealing with very short streams where variable stripping may be confused for a subhalo impact. Finally, we comment that substructure in streams can be due to incorrect modelling of the background or variable extinction but these are not issues with the stream modelling so do not concern us here.

The formalism presented promises to be crucial for constraining the properties of a subhalo fly-by on a cold stream. It is anticipated that one would find potential gap candidates in star counts as has been demonstrated by Carlberg & Grillmair (2013) and then one would follow up with more detailed observations of the kinematic structure of the gap. Erkal & Belokurov (2015b) discussed what range of subhalo properties one could potentially constrain with a current and future observation quality. They found that the shape of the gap encodes the subhalo properties and showed that with ongoing surveys like the Dark Energy Survey and *Gaia*, it will be possible to characterize dark subhaloes down to  $10^7 M_\odot$ . This analysis was limited to streams on near-circular orbits but it is anticipated that many of the insights apply to more general stream geometries. We may yield stronger constraints using stream progenitors on eccentric orbits but this remains to be seen from future analysis.

In this paper we have analysed the effect of a single subhalo fly-by. Yoon et al. (2011) have predicted that a stream such as Palomar-5 would only experience a few  $10^7$ - $10^8 M_\odot$  subhalo impacts but that there are many more much lower mass impacts. We have shown that a clear gap forms for the high mass impacts but it would be interesting to investigate the properties of the stream that has experienced many small mass subhalo impacts. In this regime we begin probing the mass spectrum of dark matter subhalos. Carlberg & Grillmair (2013) Ngan & Carlberg (2014) have discussed the effects of many small impacts from simulation but in order to constrain the mass spectrum we require full models of perturbed streams.

The framework presented here is appropriate for when an interaction between the stream and a subhalo is short compared to the orbital time of the stream such that the impulse approximation is appropriate. Instead of a full perturbative analysis we were able to simply consider instantaneous changes to the stream properties. However, it is potentially a small starting step to developing a scheme to handle more general perturbations to streams. The assumption of a smooth analytic galaxy model is probably inappropriate, particularly over the timescales on which streams evolve. Bonaca et al. (2014) presented a study of analysing streams from the Via Lactea simulation under assumptions on the smoothness of the halo and found that XXX. Additionally, recent results suggest that the mass of the LMC is much larger than previously believed (Kallivayalil et al. 2013; Peñarrubia et al. 2015). However, a counter to this is that many of the observed streams are very simple cold structures suggesting that the approximation of a smooth halo for the Milky Way is valid. Nonetheless it may be inevitable that

one has to include perturbations on top of a smooth model to fit the known streams in the Galaxy and the angle-action framework is ideal for such an endeavour. These variables were originally introduced to handle perturbative solutions to the equations of the motion in the Solar system so seem highly appropriate for handling perturbations on Galactic scales.

## ACKNOWLEDGEMENTS

JLS acknowledges the support of the Science and Technology Facilities Council.

## REFERENCES

- Bonaca A., Geha M., Kuepper A. H. W., Diemand J., Johnston K. V., Hogg D. W., 2014, ArXiv e-prints
- Bovy J., 2014, ApJ, 795, 95
- Bowden A., Belokurov V., Evans N. W., 2015, MNRAS, 449, 1391
- Carlberg R. G., 2009, ApJL, 705, L223
- Carlberg R. G., 2012, ApJ, 748, 20
- Carlberg R. G., Grillmair C. J., 2013, ApJ, 768, 171
- Diemand J., Kuhlen M., Madau P., Zemp M., Moore B., Potter D., Stadel J., 2008, Nature, 454, 735
- Erkal D., Belokurov V., 2015a, MNRAS, 450, 1136
- Erkal D., Belokurov V., 2015b, MNRAS, 450, 1136
- Eyre A., Binney J., 2011, MNRAS, 413, 1852
- Gibbons S. L. J., Belokurov V., Evans N. W., 2014, MNRAS, 445, 3788
- Helmi A., White S. D. M., 1999, MNRAS, 307, 495
- Hernquist L., 1990, ApJ, 356, 359
- Kallivayalil N., van der Marel R. P., Besla G., Anderson J., Alcock C., 2013, ApJ, 764, 161
- Koposov S. E., Rix H.-W., Hogg D. W., 2010, ApJ, 712, 260
- Küpper A. H. W., Balbinot E., Bonaca A., Johnston K. V., Hogg D. W., Kroupa P., Santiago B. X., 2015, ApJ, 803, 80
- Küpper A. H. W., Kroupa P., Baumgardt H., Heggie D. C., 2010, MNRAS, 401, 105
- Law D. R., Majewski S. R., 2010, ApJ, 714, 229
- Ngan W. H. W., Carlberg R. G., 2014, ApJ, 788, 181
- Peñarrubia J., Gómez F. A., Besla G., Erkal D., Ma Y.-Z., 2015, ArXiv e-prints
- Sanders J. L., 2014, MNRAS, 443, 423
- Sanders J. L., Binney J., 2013a, MNRAS, 433, 1813
- Sanders J. L., Binney J., 2013b, MNRAS, 433, 1826
- Sanders J. L., Binney J., 2014, MNRAS, 441, 3284
- Siegal-Gaskins J. M., Valluri M., 2008, ApJ, 681, 40
- Springel V., 2005, MNRAS, 364, 1105
- Springel V. et al., 2008, MNRAS, 391, 1685
- Tremaine S., 1999, MNRAS, 307, 877
- Williams A. A., Evans N. W., Bowden A. D., 2014, MNRAS, 442, 1405
- Yoon J. H., Johnston K. V., Hogg D. W., 2011, ApJ, 731, 58

**APPENDIX A: VELOCITY KICKS FROM A HERNQUIST SPHERE**

The potential of a Hernquist sphere (Hernquist 1990) is given by

$$\Phi_H(r) = -\frac{GM}{r + r_s}, \quad (\text{A1})$$

where  $M$  is the mass and  $r_s$  the scale radius. The velocity kicks are given by

$$\delta \mathbf{v}_{i,H}^g = -\frac{2GM}{|\mathbf{w}_i|} \frac{\mathbf{b}_i - \hat{\mathbf{w}}_i(\mathbf{b}_i \cdot \hat{\mathbf{w}}_i)}{(B^2 - r_s^2)} \left(1 - \frac{2r_s}{r_s + B} X(S)\right), \quad (\text{A2})$$

where

$$S = \sqrt{\frac{2B}{r_s + B}}, \quad (\text{A3})$$

and we have made use of the function  $X(s)$  introduced in equation (33) and (34) of Hernquist (1990) which is given by

$$X(s) = \begin{cases} \frac{1}{\sqrt{1-s^2}} \operatorname{arcsech} s, & 0 \leq s \leq 1 \\ \frac{1}{\sqrt{s^2-1}} \operatorname{arcsec} s, & 1 \leq s \leq \infty. \end{cases} \quad (\text{A4})$$

We note the form is very similar to the Plummer kicks and, as required, the two are equal when  $r_s \rightarrow 0$ .